Journal of
Materials Chemistry A

Accepted Manuscript

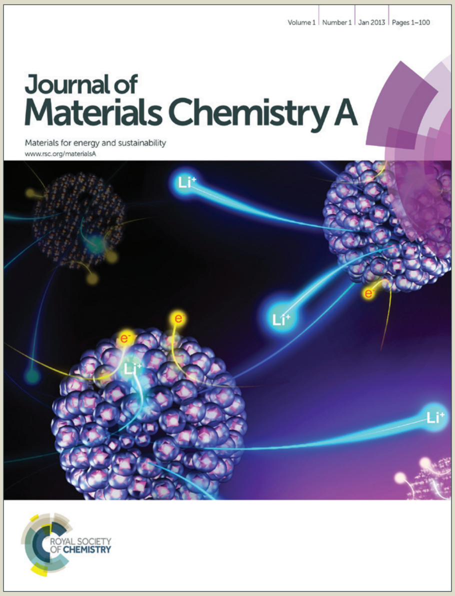

ROYAL SOCIETY
OF CHEMISTRY

www.rsc.org/materialsA

Uniform core-shell structured magnetic mesoporous TiO_2 nanospheres as a highly efficient and stable sonocatalyst for degradation of bisphenol-A

Pengpeng Qiu,[1‡] Wei Li,[2‡] Binota Thokchom,[1] Beomguk Park,[1] Mingcan Cui,[1] Dongyuan Zhao[2]* and Jeehyeong Khim [1]*

[1]School of Civil Environmental and Architecture Engineering, Korea University, Seoul 136-701, Republic of Korea

[2] Laboratory of Advanced Materials and Department of Chemistry, Fudan University, Shanghai 200433, China

*E-mail: hyeong@korea.ac.kr, dyzhao@fudan.edu.cn

[‡]The contribution is equal.

Uniform core-shell structured magnetic mesoporous TiO_2 (Fe_3O_4@SiO_2@mTiO_2) nanospheres have been fabricated *via* a kinetic-controlled Stöber method. A silica interlayer with a thickness of ~ 25 nm was introduced as a passivation barrier to prevent the photodissociation, as well as increase the thermal stability of the core-shell materials. After being crystallized at 600 °C under nitrogen, the resultant nanospheres (Fe_3O_4@SiO_2@mTiO_2-600) possess well-defined core-shell structures with a high magnetic susceptibility (~ 17.0 emu g^{-1}) and exhibit uniform mesopores (~ 5.2 nm), large BET surface area (~ 216 m^2 g^{-1}) and pore volume (~ 0.20 cm^3 g^{-1}). More importantly, the magnetic mesoporous TiO_2 has been demonstrated for the first time as a high efficient and stable sonocatalyst for the degradation of bisphenol-A. The pseudo first-order-reaction constant of the magnetic mesoporous TiO_2 is measured to be 0.164 min^{-1}, which is 1.49 and 2.27 times higher than that of P25 and ultrasound alone, respectively. The remarkable performance is attributed to the fast mass diffusion, large adsorption rate and enhanced hydroxyl-radical-production rate. More importantly, the catalysts can be easily recycled within 2 minutes by using an external magnetic field and a constant catalytic activity is retained even after eight cycles. This study paves a promising way for the design and synthesis of magnetic separable sonocatalysts for the degradation of organic pollutants, which is of significant importance for practical applications from both environmental and industrial points of view.

Introduction

Bisphenol A (BPA) is an important organic chemical that is widely used as a monomer for the production of polycarbonate plastics such as baby bottles and as a major component of epoxy resins for lining of food cans and dental sealants. It is a ubiquitous environmental micro-contaminant with endocrine disruption potential to the eco-system and human health by interfering in growth, development, and reproduction, even at very low level concentrations.[1] To some extent, BPA can be eliminated through traditional physical, chemical, or biological treatments. However, the removal efficiency is generally unsatisfactory because phenols are relatively hydrophilic and persistent to microorganisms, thus less vulnerable to traditional techniques.[2, 3] Recently, advanced oxidation processes (AOPs) have been demonstrated as a high efficient technology for the destruction and mineralization of organic micropollutants through powerful reactive oxidation species such as hydroxyl radicals. As an alternative to conventional AOPs such as ozonation, photolysis, Fenton process and photocatalytic oxidation, sonolysis is of great interest and importance because it is environment-friendly and simply operating.[4, 5] When ultrasound (US) is irradiated into aqueous phase, acoustic cavitation including the formation, growth, and violent collapse of microbubbles occurs, leading to the generation of sonoluminescence and “hot spots” with extremely high temperatures (5000 K) and pressures (1000 atm).[6-8] As a result, water is pyrolyzed to generate hydroxyl radicals, which can finally oxidize organic pollutants into CO_2 and H_2O. However, a significant amount of electric energy, costly equipment, and long irradiation time is typically required to obtain a high ultrasonic degradation rate by using onefold US, which hinders its wide application for practical water treatment.[9] To this end, addition of a heterogeneous sonocatalyst is one of the most critical and promising approach. Among various sonocatalysts, TiO_2 nano-materials are widely investigated because of their outstanding properties such as low-cost, environmental benignity, plentiful polymorphs, good chemical and thermal stability, and excellent electronic and optical properties.[10] More importantly, it has been demonstrated that TiO_2 nano-materials exhibited high sonocatalytic activities for degradation of organic pollutants due to the synergistic effect between US and TiO_2.[11-14] For example, Song *et al*.[11] fabricated a trigonal TiO_2 nanoflake, which showed a high sonocatalytic degradation rate of Rhodamine B. Ghows *et al*.[12] have reported the synthesis of core-shell structured CdS/TiO_2 for an exceptional sonocatalytic degradation of reactive black 5. Wang *et al*.[14] prepared Au loaded TiO_2 sonocatalysts, exhibiting a great acceleration in both the discoloration and total organic carbon (TOC) removal rate of azo dyes. However, the low surface area and small pore volume of TiO_2 nanocrystals still greatly hinder the sonocatalytic performance due to the limited mass transfer, adsorption and surface nucleation process. In addition, the separation of TiO_2 nanocystals from the catalytic system is difficult.

Recently, mesoporous TiO_2 materials have been received increasing attention owing to their fascinating properties such as high surface areas, large pore volumes and uniform mesopore channels that can not only extraordinarily increase the density of accessible active sites, but also greatly facilitate mass diffusion within frameworks.[15-20] As a result, mesoporous TiO_2 exhibits substantial performance boosts in numerous applications such as lithium-ion insertion, catalysis, photovoltaic cells and so on.[21-23] However, up to now, the investigation of mesoporous TiO_2 as an advanced sonocatalyst has rarely been reported.[24] In addition, another major obstacle remaining in the application of nanosized sonocatalysts is the separation of nanoparticles from a complex heterogeneous system for recycling. This challenge greatly hinders their practical and widespread applications. Magnetic separation provides a very convenient approach for removing and recycling magnetic particles such as magnetite, ferrite, and barium ferrite by applying external magnetic fields.[25-27] The incorporation of magnetic components into TiO_2 based catalysts can greatly enhance the separation and recovery of nanosized TiO_2.[28] However, a direct contact between magnetic iron oxide and TiO_2 usually gives rise to an unfavorable heterojunction during heat treatment and an increase in electron-hole recombination and photodissolution under light, thus decreasing the photo efficiency and life time of the resultant material.[29-30] Therefore, the investigation of mesoporous TiO_2 with a high surface area, superior magnetic recyclable properties and high stability as an advanced sonocatalyst is greatly desired.

Herein, uniform core-shell structured magnetic mesoporous TiO_2 nanospheres ($Fe_3O_4@SiO_2@mTiO_2$) have been fabricated *via* a kinetically controlled Stöber method. The introduction of a rigid silica layer between Fe_3O_4 core and TiO_2 shell is to help prevent the photodissociation and inhibit the electron-hole recombination, as well as increase the thermal stability of the resultant core-shell material. After crystallized at 600 °C under N_2, the magnetic mesoporous TiO_2 nanospheres possess a high surface area (~ 200 m^2 g^{-1}), a large pore size (~ 5.4 nm), and a high magnetic susceptibility (~ 17.0 emu g^{-1}). The magnetic mesoporous nanospheres are used as a sonocatalyt for degradation of bisphenol-A and exhibit a high degradation rate constant (0.164 min^{-1}), which is 2.05 and 1.49 times higher than that of nonporous one (0.08 min^{-1}) and the one without silica protection (0.142 min^{-1}), respectively. Moreover, the excellent catalysts can be easily recycled within 2 minutes by using an external magnetic field and the constant activity is retained even after eight cycles.

Experimental Section

Materials

$FeCl_3 \cdot 6H_2O$, trisodium citrate, ethylene glycol, sodium acetate, tetraethyl orthosilicate (TEOS), titanium (IV) isopropoxide (TIPO), ethanol, concentrated ammonia solution (28 wt%) and BPA were of analytical grade and purchased from Sigma-Aldrich (USA). Potassium bi-phthalate (C_6H_4 COOK COOH, 99.7 %), ammonium molybdate ($(NH_4)_6Mo_7O_{24} \cdot 4H_2O$, 99.0 %), sodium hydroxide (NaOH, 99.0 %) and potassium iodide (KI, 99.5 %) were obtained from Samchun Company (Korea). All chemicals were used as received without further purification. Millipore water was used for all experiments.

Synthesis of Fe_3O_4 nanoparticles.

The water-dispersible Fe_3O_4 nanoparticles were synthesized *via* a solvothermal method reported previously.[31] Briefly, $FeCl_3 \cdot 6H_2O$ (3.25 g), trisodium citrate (1.3 g), and sodium acetate (NaAc, 6.0 g) were dissolved in ethylene glycol (100 mL) with magnetic stirring. Afterwards, the obtained yellow solution was transferred and sealed into a Teflon-lined stainless-steel autoclave (100 mL in capacity). The autoclave was heated at 200 °C for 10 h, and then allowed to cool to room temperature. The black products were washed with deionized water and ethanol for 3 times, respectively.

Synthesis of core-shell $Fe_3O_4@SiO_2$ nanospheres.

The core-shell $Fe_3O_4@SiO_2$ nanospheres were prepared through a versatile Stöber sol-gel method. For a typical synthesis, an ethanol dispersion of the Fe_3O_4 magnetite particles obtained above (3.0 mL, 0.05 g/mL) was added to a three-neck round-bottom flask with ethanol (280 mL), deionized water (70 mL) and concentrated ammonia solution (4.0 mL, 28 wt%). The mixed solution was sonicated for 15 min. Then, 2.0 mL of TEOS was added dropwise in 10 min, and the reaction was allowed to proceed for 10 h at room temperature under continuous mechanical stirring. The resultant products (denoted as Fe_3O_4@SiO_2) were separated and collected with a magnet, followed by washing with deionized water and ethanol for 3 times, respectively.

Synthesis of uniform mesoporous TiO_2 core-shell nanostructure.

The uniform mesoporous TiO_2 shell structures were prepared via an extended Stöber method.[32] Typically, the core-shell Fe_3O_4@SiO_2 nanospheres were dispersed in ethanol (100 mL), and mixed with concentrated ammonia solution (0.40 mL, 28 wt%) under ultrasound for 15 min. Subsequently, 0.75 mL of TIPO was added dropwise in 5 min, and the reaction was allowed to proceed for 24 h at 45 °C under continuous mechanical stirring. The resultant products (denoted as Fe_3O_4@SiO_2@TiO_2) were separated and collected, followed by an additional ultrasonic post-hydrolysis process in water, according to that reported previously.[33] The obtained mesoporous TiO_2 core-shell nanospheres were denoted as Fe_3O_4@SiO_2@mTiO_2. Finally, the resultant samples were collected with a magnet and calcined at 600 °C under nitrogen for 2 h to remove the organic species and improve crystallinity (designated as Fe_3O_4@SiO_2@mTiO_2-600). The overall synthesis strategy for the core-shell magnetic mesoporous TiO_2 nanospheres is depicted in Fig.1**.**

For comparison, nonporous Fe_3O_4@SiO_2@TiO_2-600 core-shell nanospheres were synthesized through directly annealing the Fe_3O_4@SiO_2@TiO_2 samples without additional ultrasound assisted post-hydrolysis process. Fe_3O_4@mTiO_2-600 nanostructure was prepared by a similar procedure without the silica layer coating. For a typical synthesis, an ethanol dispersion of the Fe_3O_4 magnetite particles (3.0 mL, 0.05 g mL^{-1}) was dispersed in ethanol (100 mL), and mixed with concentrated ammonia solution (0.40 mL, 28 wt%) under ultrasound for 15 min. Subsequently, 0.75 mL of TIPO was added dropwise in 5 min, and the reaction was allowed to proceed for 24 h at 45 °C under continuous mechanical stirring. The post treatments were same as that for the preparation of the Fe_3O_4@SiO_2@mTiO_2-600 nanospheres.

Materials characterization.

X-ray diffraction (XRD) patterns were recorded on a Bruker D8X-ray diffractometer with Ni-filtered Cu Kα radiation (40 kV, 40 mA). X-ray photoelectron spectroscopy (XPS) experiments were carried out on a PHI-5000 VersaProbeTM ULVAC system (Japan) with Al K monochromatic radiation (hυ = 1486.6 eV). Nitrogen sorption isotherms were measured at 77 K with a Micromeritics Tristar 3020 analyzer (USA). Prior to measurements, the samples were degassed in a vacuum at 180 °C for 6 h. The Brunauer-Emmett-Teller (BET) method was utilized to calculate the specific surface areas (SBET) using adsorption data in the relative pressure range $P/P_0 = 0.04 – 0.2$. Using the Barrett-Joyner-Halenda (BJH) model, the pore size distributions were derived from the adsorption branches of the isotherms, and the total pore volumes (V) were estimated from the adsorbed amount at the relative pressure P/P0 of 0.995. Transmission electron microscopy (TEM) was carried out on a JEOL 2011 microscope (Japan) operated at 200 kV. For TEM measurements, the sample was suspended in ethanol and supported on a holey carbon film on a Cu grid. The magnetization was measured using a Vibrating Sample Magnetometer (EV9 including auto-matic sample rotation, Microsense, Japan) under a magnetic field of 10 KOe and a temperature of 24 °C.

Sonocatalytic degradation measurements.

The sonoreactor consisted of a double-layered cylindrical container with a capacity of 1.25 L (Φ 10.0 × 16.0 cm), and was equipped with a cup–horn-type ultrasonic transducer (Mirae Ultrasonic

MEGA-100) (Fig. S1). The frequency of 300 kHz and maximum power of 100 W were applied for proceeding the sonocatalytic reaction. A 800-mL reactor (Φ 7.0 × 20.0 cm) was emerged into the container loaded with 500 mL of water for the reaction. The solution temperature was measured using a thermometer (Tecpel DTM-318) and maintained with a water jacket. A retort stand was used to fix the emerged reactor. The distance between the bottom of the reactor and container was about 6.0 cm. Aqueous suspensions (100 mL) of BPA (5 mg L^{-1}) and catalyst (0.5 g L^{-1}) were used for the sonocatalytic degradation. At given time intervals, 0.5 mL of the suspension was removed using a 2-mL syringe and filtered by a membrane with a pore size of ~ 0.45 µm. The BPA concentration in the resultant filtrate was analyzed on a High-performance Liquid Chromatography (HPLC, Agilent 1260) with a ZORBAX Eclipse Plus C18 column (4.6×100 mm, 5 µm) and a diode array UV detector (G4212B 1260 DAD, λ = 222 nm). The environmental conditions of HPLC for analyzing BPA were controlled according to the previous report.[34] The TOC concentration was measured using a laboratory TOC analyzer (SIEVERS 5310C).

Hydroxyl radial and leached iron measurements.

The detection of generated H_2O_2 was used as an indirect method to confirm the concentration of hydroxyl radicals, which was described by Beckett and Hua *et al.*[35] Typically, 1000 mL of A solution dissolved with KI (66 g), NaOH (2.0 g) and $(NH_4)_6Mo_7O_{24}\cdot4H_2O$ (2.0 g), and 1000 mL of B solution containing 10 g of $C_6H_4COOKCOOH$ was prepared and stirred for 24 h. A mixed solution of 0.5 mL/1 mL/0.5 mL (A solution/sample/B solution) was added to a 10-mL tube orderly. The mixed solution was diluted by adding 2.0 ml of water and stirred quickly for 10 sec before the absorbance was measured. The concentration of H_2O_2 was measured at absorption band maximum of 350 nm using the ThermoSpectronic UV 500 UV-visible spectrometer.

Leached iron ions were measured by an Inductively Coupled Plasma Atomic Emission Spectrometer (ICP-AES; Perkin Elmer 5300DV).

Results and discussion

Characterization.

The uniform magnetite particles can be synthesized *via* a facile solvothermal reaction based on a high temperature reduction of Fe (III) salts with ethylene glycol in the presence of trisodium citrate. The obtained Fe_3O_4 particles possess a uniform spherical shape with an average diameter of ~ 130 nm (Fig. 2A and B). The particles exhibit excellent dispersibility in polar solvents such as water and ethanol because of numerous citrate groups anchored on the surface, facilitating the subsequent coating with silica and titania. The $Fe_3O_4@SiO_2$ nanospheres after the first sol-gel coating process show a relatively smooth surface with a diameter of ~ 180 nm (Fig. 2C and D). TEM images reveal that a silica layer with a thickness of ~ 25 nm is uniformly coated onto the magnetic core, resulting in a well-defined core-shell structure. The further sol-gel coating process leads to the formation of sandwich-like $Fe_3O_4@SiO_2@TiO_2$ nanospheres with an average diameter of 250 nm, indicating the presence of ~ 35 nm thick TiO_2 layer (Fig. S2A and B). However, TEM images of the as-made $Fe_3O_4@SiO_2@TiO_2$ nanospheres clearly show the presence of linkage between adjacent nanospheres and tear junctions on the surface of TiO_2 shells. After the ultrasonic post-hydrolysis process, uniform and monodispersed mesoporous $Fe_3O_4@SiO_2@mTiO_2$ nanospheres are obtained (Fig. 3A and B). TEM images unambiguously demonstrate that the previous smooth surface of the TiO_2 shells is converted into a rough one and the linkage is disappeared. More importantly, the TiO_2 shells exhibit highly mesoporous structures, which are resulted from the voids between the aggregated TiO_2 oligomers. N_2 sorption isotherms of the core-shell $Fe_3O_4@SiO_2@mTiO_2$ nanospheres show a characteristic IV curve with a hysteresis loops close to H_1-type and an increase in the adsorption branch at a relative pressure of $P/P_0 = 0.3\text{-}0.5$, further suggesting that the TiO_2 shells contain uniform mesopores (Fig. 4A). The BET surface area and pore volume of the Fe_3O_4@SiO_2@mTiO_2 nanospheres are calculated to be 384 $m^2\ g^{-1}$ and 0.36 $cm^3\ g^{-1}$, respectively, which are much higher than that of nonporous Fe_3O_4@SiO_2@TiO_2 sample (106 $m^2\ g^{-1}$, 0.2 $cm^3\ g^{-1}$) (Table S1). Moreover, the corresponding pore size distribution curve (Fig. 4B) of the core-shell Fe_3O_4@SiO_2@mTiO_2 nanospheres derived from the adsorption branch of the isotherms by using the BJH model clearly reveals a uniform pore size of ~ 3.5 nm, larger than that of nonporous Fe_3O_4@SiO_2@TiO_2 nanospheres (< 1.5 nm).

Notably, when the core-shell Fe_3O_4@SiO_2@mTiO_2 samples after being calcined at 600 °C in nitrogen, discrete and uniform nanospheres are well retained (Fig. 3C and D). The HRTEM image (Fig. 3F) clearly displays that the TiO_2 nanoparticles are well crystallized with a size of ~ 5.5 nm and a *d-spacing* of 0.35 nm, well-matching to the d_{101} of anatase.[36] Energy-dispersive X-ray (EDX) of the core-shell Fe_3O_4@SiO_2@mTiO_2-600 nanospheres (Fig. 3E) exhibits the characteristic peaks of titanium (14.72%), carbon (40.88%), oxygen (42.90%) and silica (1.50%) (Table S2), suggesting that the Fe_3O_4@SiO_2 cores are well coated by mesoporous TiO_2 shells. However, when the core-shell Fe_3O_4@SiO_2@TiO_2 samples are directly annealed without the post-hydrolysis process, the resultant nanospheres appear to be aggregated together and the surface of TiO_2 shells is cracked, which may be induced by the external forces (Fig. S2C and D). The HRTEM image (Fig. S2D inset) clearly reveals that the size of TiO_2 nanocrystals is approximately 10.0 nm. The BET surface area and pore volume of the Fe_3O_4@SiO_2@mTiO_2-650 are calculated to be 216 $m^2\ g^{-1}$ and 0.20 $cm^3\ g^{-1}$, respectively, much higher than that of nonporous one (25.6 $m^2\ g^{-1}$, 0.048 $cm^3\ g^{-1}$). The corresponded pore-size distribution curve clearly shows a uniform pore size of ~ 5.2 nm, while the sample Fe_3O_4@SiO_2@TiO_2-600 has a wide pore size distribution (Fig. 4B). In contrast, when annealing Fe_3O_4@mTiO_2 sample without the silica layer coating, the well-defined core-shell structures are disappeared and some nanospheres are obviously broken (Fig. S3), perhaps resulted from the recrystallization of Fe_3O_4. Black spots attributed to Fe element are clearly observed in the TiO_2 shells (Fig. S3C and D). Moreover, the EDX analysis taken at red square displays a sharp and intense typical characteristic peak of Fe, confirming the diffusion of some iron atoms into TiO_2 shells.

The XRD pattern (Fig. 5) of the Fe_3O_4@SiO_2 nanospheres displays several broad characteristic diffraction peaks, which are typical for amorphous silica and Fe_3O_4 crystalline phase, respectively. Compared with the sample Fe_3O_4@SiO_2, diffraction peaks attributed to the TiO_2 anatase are also detected in the XRD patterns of the core-shell Fe_3O_4@SiO_2@TiO_2-600 and Fe_3O_4@SiO_2@mTiO_2-600 nanospheres. Clearly, anatase characteristic peaks of Fe_3O_4@SiO_2@mTiO_2-600 nanospheres are much weaker than those of the Fe_3O_4@SiO_2@TiO_2-600 samples. By using the Scherrer formula, the average crystal sizes of TiO_2 anatase are estimated to be ~ 5.5 and 10 nm, respectively, in good agreement with the TEM results. Interestingly, the XRD pattern of the core-shell Fe_3O_4@mTiO_2-600 sample shows intense crystalline diffraction peaks at $2\theta = 23.8, 32.6, 35.2, 40.4, 49.9, 53.1, 62.6$ and $63.3°$, in accordance with $FeTiO_3$ (JCPDS, 75-0519), which is clearly different from that of the sample with the silica layer, further indicating the stabilization effect of silica interlayer towards Fe_3O_4 core during calcination. XPS analysis was used to investigate the surface element of the resultant core-shell nanospheres. The survey spectra (Fig. 6) of the core-shell Fe_3O_4@SiO_2 shows three well-resolved peaks of Si 2s, Si 2p and O 1s without the typical one of Fe element, further suggesting that the Fe_3O_4 cores are uniformly coated by a smooth silica layer. Similarly, no typical silica peak (Fig. S4 A) is detected in the spectra of the sample Fe_3O_4@SiO_2@mTiO_2-600, demonstrating that the Fe_3O_4@SiO_2 cores are well encapsulated by mesoporous TiO_2 shells. However, in XPS spectra of the sample Fe_3O_4@mTiO_2-600 without the silica layer, a sharp and intense Fe 2p peak (Fig. S4 B) appears, indicating the diffusion of iron atoms into the TiO_2 shells and the formation of $FeTiO_3$, which is in consistent with the results of TEM and XRD. These results imply that the presence of silica interlayer can greatly improve the thermal stability of the resultant core-shell materials during calcination. Clearly, the magnetization saturation values of pristine Fe_3O_4 particles, Fe_3O_4@SiO_2, and Fe_3O_4@ SiO_2@mTiO_2-600 are measured to be ~58.4, 35.0, and 17.0 emu/g, respectively (Fig. 7). As a result of the superparamagnetic property and high magnetization, the core-shell Fe_3O_4@SiO_2@mTiO_2-600 nanospheres in their homogeneous dispersion show fast motion under the applied magnetic field and quick dispersibility upon a slight shake when the magnetic field is removed (Fig. 7 inset).

Sonocatalytic performance.

The performance of the resultant core-shell materials on the sonocatalytic degradation of BPA was examined (Fig. 8). As a control, the sonocatalytic performances of US alone and commercial TiO_2 nanoparticles P25 were also tested, exhibiting the degradation rate constants of 0.072 and 0.11 min^{-1}, respectively, when a pseudo first-order reaction was assumed. It further proves that P25 can perform as a good sonocatalyst for accelerating the ultrasonic degradation rate of organic pollutants. Interestingly, the nonporous core-shell Fe_3O_4@SiO_2@TiO_2-600 sample shows a much smaller degradation constant (0.082 min^{-1}) than that of P25, due to the low BET surface area, small pore volume (Table S1) and low content of TiO_2. When the magnetic core-shell mesoporous TiO_2 samples were used as a sonocatalyst, the sonocatalytic degradation performance was unambiguously improved. The pseudo first-order degradation constant of the core shell nanospheres Fe_3O_4@SiO_2@mTiO_2-600 sonocatalyst is measured to be 0.164 min^{-1}, which is 2.27 and 1.49 times as higher as that of US and P25, respectively. As a comparison, we found that the magnetic mesoporous TiO_2 without the silica layer coating displayed a slightly smaller reaction rate constant of 0.142 min^{-1}, which was possibly resulted from the heterostructured $FeTiO_3$/TiO_2 composites possessing faster electron-hole recombination rate.[28,37] TOC analyses were examined to evaluate the mineralization performance of the resultant material (Fig. S5). Clearly, the Fe_3O_4@SiO_2@mTiO_2-600 sonocatalyst possesses more effective mineralization rate for BPA removal (48.2 % removal in 8 h) than that of US (15.1 %) and p25 (29.3 %), further indicating the outstanding catalytic property of magnetic mesoporous TiO_2. The remarkable sonocatalytic performance of the core-shell Fe_3O_4@SiO_2@mTiO_2-600 can be attributed to the fast mass diffusion, large adsorption rate and enhanced hydroxyl-radical-generation rate. The adsorption kinetic plots (Fig. S6A) clearly reveal that no apparent adsorption is found in the presence of P25 and nonporous magnetic TiO_2. However, nearly 15% of BPA could be removed in five minutes when the Fe_3O_4@SiO_2@mTiO_2-600 sonocatalyst was added, indicating the faster mass diffusion and larger amount of adsorption sites. Measurements of the generated hydroxyl radicals in the sonocatalytic system (Fig. S6B) further confirmed the catalytic effect of TiO_2 for the degradation of BPA. The hydroxyl-radical-production rate can be greatly improved after the addition of P25, which is attributed to the formation of electron-holes pairs with the excitation of sonoluminescence and heat emitted by the collapsed bubbles.[38, 39] More importantly, both of the samples Fe_3O_4@SiO_2@mTiO_2-600 and Fe_3O_4 @mTiO_2-600 exhibit a larger production rate than P25 and Fe_3O_4@SiO_2@TiO_2-600, respectively, indicating that the uniform mesoporous structures in the resultant materials play an important role in the generation rate of hydroxyl radicals. Previous studies have shown that the nucleation of a microbubble within a pore is faster than that of a flat or smooth surface because pore corners provide energetically preferred binding sites at which the new phase can be formed.[40-42] In this case, the magnetic TiO_2 mesopore channels on the shells can provide larger amount of nucleation sites for the generation of microbubbles, thus producing superior cavitation effects to nonporous one.

The recycle test of the core-shell Fe_3O_4@SiO_2@mTiO_2-600 was tested (Fig. 9). After eight recycles, a similar reaction rate constant was retained. The excellent reusability is ultimately related to the high magnetization and superior sono-stability. The weight loss plots (Fig. S7a) clearly revealed that almost constant catalyst weight (> 94% of total catalyst weight) can be collected at each recycle due to the high magnetic collection efficiency. In addition, TEM images (Fig. S8) clearly showed that the defined core-shell structure is well retained even after eight cycles, suggesting the excellent mechanical stability of the core-shell Fe_3O_4@SiO_2@mTiO_2-600 nanospheres. However, the surface of the recycled sample became smashed compared to fresh one, which was resulted from the continuous asymmetrical pitting by the shock waves.[43] In contrast, the recycle tests for the sample Fe_3O_4@mTiO_2-600 were also carried out, exhibiting a very poor reusability. The pseudo-first order kinetic constant was degraded linearly as recycle time increased, which was resulted from the low magnetization (10 emu g^{-1}, Fig. 7) and photodissociation. The leached iron ions concentration in the resultant solution after one cycle of reaction was measured to be 0.334 mg L^{-1} (0.6 wt% of total catalysts), which was much higher than that of the sample Fe_3O_4@SiO_2@mTiO_2-600 (0.009 mg L^{-1}, 0.018 wt% of total catalysts), further indicating the importance of the silica interlayer. Notably, as a result of the low magnetic collection efficiency and photoleaching of irons, 20 wt% of the sonocatalysts was lost during eight cycles, resulting in the low recycle ability of the sample Fe_3O_4@mTiO_2-600 without coating a silica layer (Fig. S7b). The reusability tests further confirm that the core-shell $Fe_3O_4@SiO_2@mTiO_2$-600 is a promising candidate as a sonocatalyst.

Conclusions

Uniform core-shell structured magnetic mesoporous TiO_2 have successfully been fabricated *via* a kinetic-controlled Stöber method. The introduction of a silica interlayer can greatly improve the thermal and photo stability of the resultant materials. After being crystallized at 600 °C under N_2, the resultant nanospheres possess well-defined core-shell structures with a high magnetic susceptibility (~ 17.0 emu g^{-1}) and exhibit highly uniform mesopores (~ 5.2 nm), large BET surface area (~ 216 m^2 g^{-1}), and pore volume (0.20 cm^3 g^{-1}). More importantly, the magnetic mesoporous TiO_2 core-shell structures were demonstrated as a highly efficient sonocatalyst, showing a remarkable performance for the sonocatalytic degradation of bisphenol-A. The pseudo first-order sonocatalytic reaction constant of magnetic core-shell mesoporous TiO_2 nanospheres is 0.164 min^{-1}, which is 2.27 and 1.49 times as high as that of the nonporous magnetic TiO_2 and P25, respectively. Finally, the catalyst can be easily recycled within 2 minutes by using an external magnetic field and the constant activity was retained even after eight cycles. This study paved a critical way for the design and synthesis of highly efficient and stable magnetic separable sonocatalyst for the degradation of organic pollutants, which is of vital importance for practical applications from both of environmental and industrial point of view.

Acknowledgments

This work was supported by the Basic Science Research Program through a National Research Foundation of Korea (NRF) grant funded by the Ministry of Education, Science, and Technology (NRF2013R1A1A2006586), WL and DYZ thank the financial support from NSF of China (21210004).

References

1. W.-T. Tsai, *J. Environ. Sci. Health C Environ. Carcinog. Ecotoxicol. Rev.* 2006, **24**, 225−255.
2. I. Bautista-Toledo, M. A. Ferro-García, J. Rivera-Utrilla, C. Moreno-Castilla and F. J. Vegas Fernández, *Environ. Sci. Technol.* 2005, **39**, 6246−6250.
3. J. H. Kang and F. Kondo, *Chemosphere* 2002, **49**, 493−498.
4. I. Gültekin and N. H. Ince, *J. Environ. Manage.* 2007, **85**, 816−832.
5. J. L. Wang and L. J. Xu, *Crit. Rev. Environ. Sci. Technol.* 2011, **42**, 251−325.
6. P. Chowdhury and T. Viraraghavan, *Sci. Total Environ.* 2009, **407**, 2474−2492.
7. S. I. Madanshetty and R. E. Apfel, *J. Acoust. Soc. Am.* 1991, **90**, 1508−1514.
8. M. Ashokkumar and F. A. Grieser, *J. Am. Chem. Soc*. 2005**,** **127**, 5326−5327.
9. N. N. Mahamuni and Y. G. Adewuyi, *Ultrason. Sonochem.* 2010, **17**, 990−1003.
10. R. Wang, G. Jiang, Y. Ding, Y. Wang, X. Sun, X. Wang and W. Chen, *ACS Appl. Mater. Interfaces* 2011, **3**, 4154−4158.
11. L. Song, S. Zhang, X. Wu and Q. Wei, *Ultrason. Sonochem.* 2012, **19**, 1169−1173.
12. N. Ghows and M. H. Entezari, *J. Hazard. Mater*. 2011, **195**, 132−138.
13. Y. Wang, D. Zhao, W. Ma, C. Chen and J. Zhao, *Environ. Sci. Technol.* 2008, **42**, 6173−6178.
14. J. Wang, Y. Lv, Z. Zhang, Y. Deng, L. Zhang, B. Liu, R. Xu and X. Zhang, *J. Hazard. Mater*. 2009, **170**, 398−404.
15. W. Li, Z. Wu, J. Wang, A. A. Elzatahry and D. Zhao, *Chem. Mater.* 2013, **26**, 287−298.
16. J. Wang, H. Li, H. Li, C. Zou, H. Wang and D. Li, *ACS Appl. Mater. Interfaces* 2014, **6**, 1623−1631.

17. S. Agarwala, M. Kevin, A. S. W. Wong, C. K. N. Peh, V. Thavasi and G. W. Ho, *ACS Appl. Mater. Interfaces* 2010, **2**, 1844−1850.

18. W. Weng, T. Higuchi, M. Suzuki, T. Fukuoka, T. Shimomura, M. Ono, L. Radhakrishnan, H. Wang, N. Suzuki, H. Oveisi, and Y. Yamauchi, Angew. Chem. Int. Ed. 2010, 49, 3956−3959

19. H. Oveisi, S. Rahighi, X. Jiang, Y. Nemoto, A. Beitollahi, S. Wakatsuki, and Y. Yamauchi, *Chem. Asian J.*, 2010, **5**, 1978-1983.

20. K. C.-W. Wu, Y. Yamauchi, C. Y. Hong, Y. H. Yang, Y. H. Liang, T. Funatsu and M.Tsunoda. Chem. Commun., 2011,47, 5232–5234.

21. R. Zhang, A. A. Elzatahry, S. S. Al-Deyab and D. Zhao, *Nano Today* 2012, **7**, 344−366.

22. R. Zhang, D. Shen, M. Xu, D. Feng, W. Li, G. Zheng, R. Che, A. A. Elzatahry and D. Zhao, *Adv. Energy Mater.* 2014, **4**, 1301725−1301725.

23. W. Zhou, W. Li, J.-Q. Wang, Y. Qu, Y. Yang, Y. Xie, K. Zhang, L. Wang, H. Fu and D. Zhao, *J. Am. Chem. Soc*. 2014, **136**, 9280−9283.

24. P. Qiu, W. Li, K. Kang, B. Park, W. Luo, D. Zhao and J. H. Khim, *J. Mater. Chem. A* 2014, **2**, 16452−16458.

25. W. Li, Y. Deng, Z. Wu, X. Qian, J. Yang, Y. Wang, D. Gu, F. Zhang, B. Tu and D.Zhao, *J. Am. Chem. Soc*. 2011, **133**, 15830−15833.

26. Y. Deng, Y. Cai, Z. Sun and D. Zhao, *Chem. Phy. Lett.* 2011, **510**, 1−13.

27. A.-H. Lu, E. L. Salabas and F. Schüth, *Angew. Chem, Int. Ed.* 2007, **46**, 1222−1244.

28. D. Beydoun, R. Amal, G. K. C. Low and S. McEvoy, *J. Phys. Chem. B* 2000, **104**, 4387−4396.

29. V. Belessi, D. Lambropoulou, I. Konstantinou, R. Zboril, J. Tucek, D. Jancik, T. Albanis and D. Petridis, *Appl. Catal., B: Environ.* 2009, **87**, 181−189.

30. L. De Matteis, R. Fernández-Pacheco, L. Custardoy, M. L. García-Martín, J. M. de la Fuente, C. Marquina and M. R. Ibarra, *Langmuir* 2014, **30**, 5238−5247.

31. J. Liu, Z. Sun, Y. Deng, Y. Zou, C. Li, X. Guo, L. Xiong, Y. Gao, F. Li and D. Zhao, *Angew. Chem. Int. Ed.* 2009, **48**, 5875−5879.

32. W. Li, J. Yang, Z. Wu, J. Wang, B. Li, S. Feng, Y. Deng, F. Zhang and D. A. Zhao, *J. Am. Chem. Soc*. 2012, **134**, 11864−11867.

33. W. Li, M. Liu, S, Feng, X. Li, J. Wang, D. Shen, Y. Li, Z. Sun, A. A. Elzatahry, H. Lu and D. Zhao, *Mater. Hori.* 2014, **1**, 439−445.

34. S. S. Lateef, Agilent Application Solution Analysis of Bisphenol A - Leaching from Baby Feeding Bottles; Agilent Technologies, Inc.

35. M. A. Beckett and I. Hua, *J. Phys. Chem. A* 2001, **105**, 3796−3802.

36. W. Li, F. Wang, S. Feng, J. Wang, Z. Sun, B. Li, Y. Li, J. Yang, A. A. Elzatahry, Y. Xia and D. Zhao, *J. Am. Chem. Soc*. 2013, **135**, 18300−18303.

37. M. Ye, Q. Zhang, Y. Hu, J. Ge, Z. Lu, L. He, Z. Chen and Y. Yin, *Chem. Eur. J.* 2010, **16**, 6243−6250.

38. H. Ogi, M. Hirao and M. Shimoyama, *Ultrason.* 2002, **40***,* 649−650.

39. T. Shinbara, T. Makino, K. Matsumoto and J. Mizuguchi, *J. Appl. Physics* 2005, **98**, 044909−044913.

40. H. Nakui, K. Okitsu, Y. Maeda and R. Nishimura, *Ultrason. Sonochem.* 2007, **14**, 191−196.

41. L. O. Hedges and S. Whitelam, *Soft Matter* 2012, **8**, 8624−8635.

42. V. Belova, D. A. Gorin, D. G. Shchukin and H. Möhwald, *ACS Appl. Mater. Interfaces* 2011, **3**, 417−425.

43. K. S. Suslick, S. J. Doktycz and E. B. Flint, *Ultrason.* 1990, **28**, 280−290.

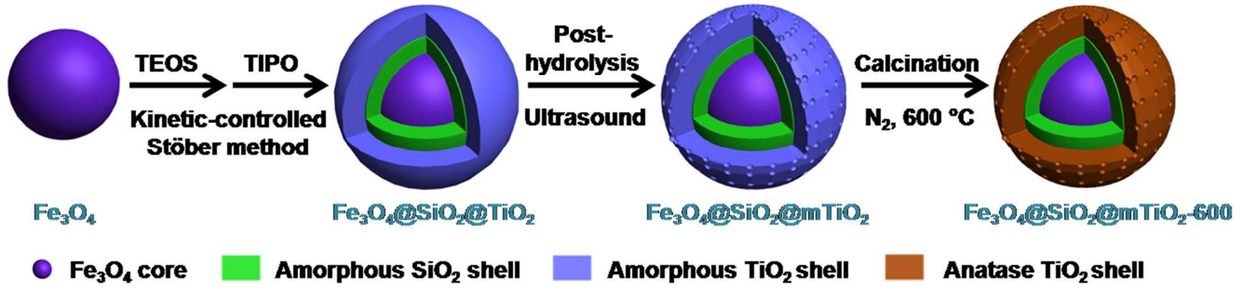

Fig. 1. Schematic illustration for the synthesis of core-shell magnetic mesoporous TiO_2.

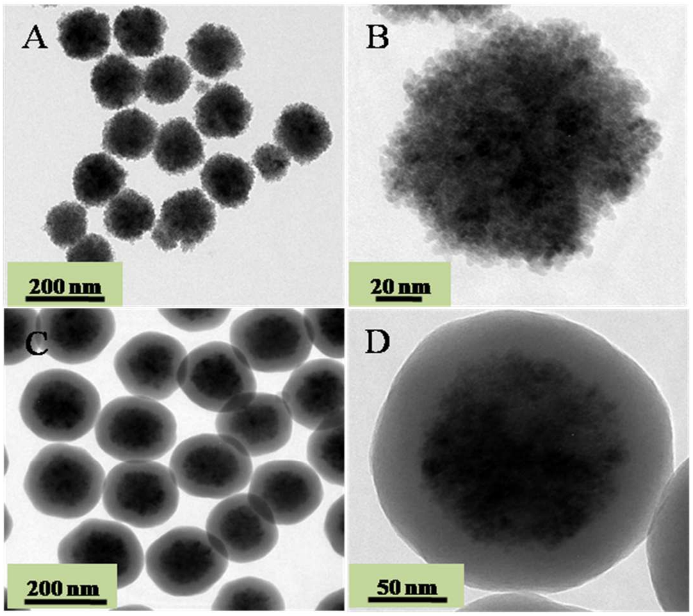

Fig. 2. TEM images of (A and B) the uniform spherical Fe_3O_4 nanoparticles prepared *via* a solventhermal method and (C and D) well-defined core-shell $Fe_3O_4@SiO_2$ nanospheres.

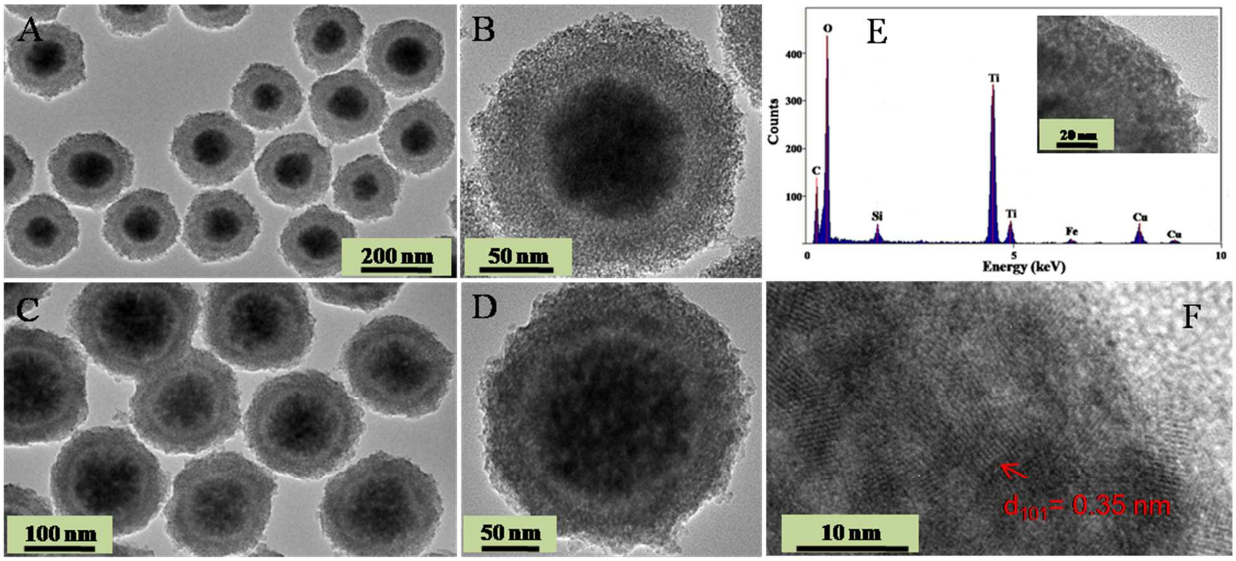

Fig. 3. TEM images of (A and B) the uniform core-shell Fe_3O_4@SiO_2@mTiO_2 nanospheres prepared *via* a modified Stöber method, followed by an ultrasound assisted post-hydrolysis route and (C and D) Fe_3O_4@SiO_2@mTiO_2-600 nanospheres obtained by annealing Fe_3O_4@SiO_2@mTiO_2 sample at 600 °C in N_2. (E) EDX analysis taken at inserted HRTEM image of mesoporous Fe_3O_4@SiO_2@mTiO_2-600 core-shell nanospheres. (F) HRTEM image of Fe_3O_4@SiO_2@mTiO_2-600 core-shell nanospheres.

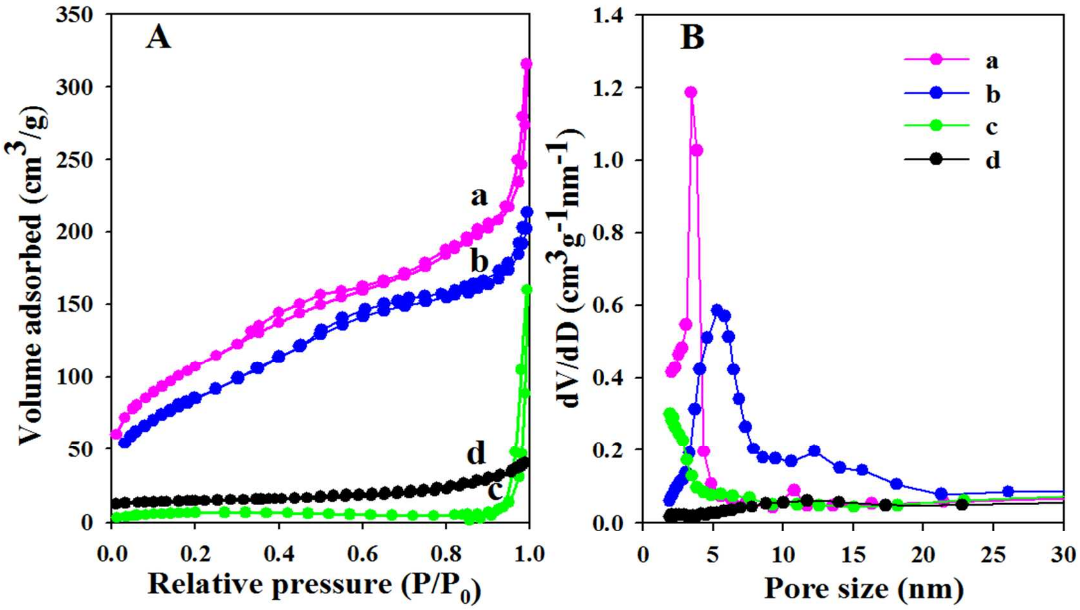

Fig. 4. (A) N_2 sorption isotherms and (B) pore-size distributions of (a) the mesoporous Fe_3O_4@SiO_2@mTiO_2 core-shell nanospheres, (b) mesoporous Fe_3O_4@SiO_2@mTiO_2-600 core-shell nanospheres, (c) bulk Fe_3O_4@SiO_2@TiO_2 core-shell nanospheres, (d) nonporous Fe_3O_4@SiO_2@TiO_2-600 core-shell nanospheres. In A, the N_2 sorption isotherms of the sample Fe_3O_4@SiO_2@TiO_2-600 are shifted vertically by 10 cm^3/g for clear observation.

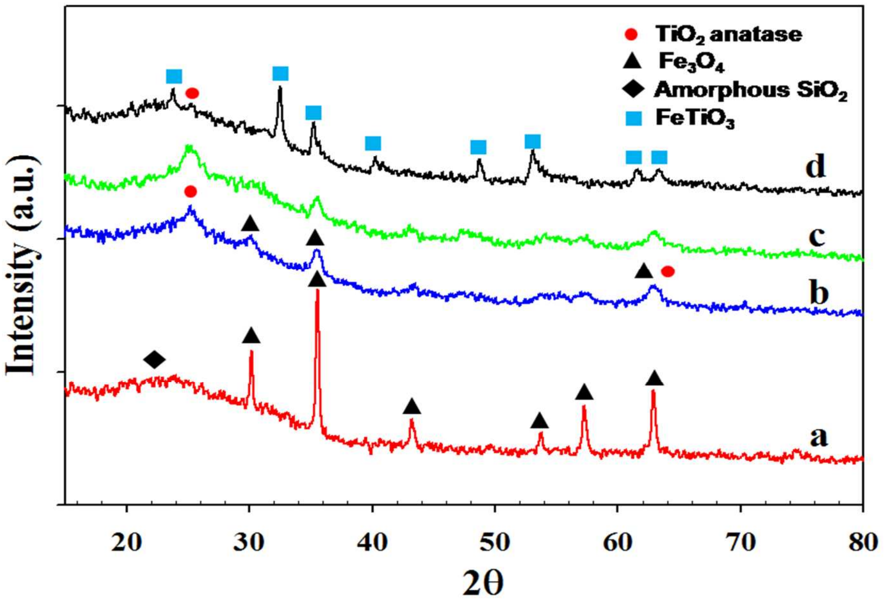

Fig. 5. XRD patterns of (a) the Fe_3O_4@SiO_2 core-shell nanospheres, (b) uniform mesoporous Fe_3O_4@SiO_2@mTiO_2-600 core-shell nanospheres, (c) nonporous Fe_3O_4@SiO_2@TiO_2-600 core-shell nanospheres, and (d) mesoporous Fe_3O_4@mTiO_2-600 core-shell nanospheres without silica layer.

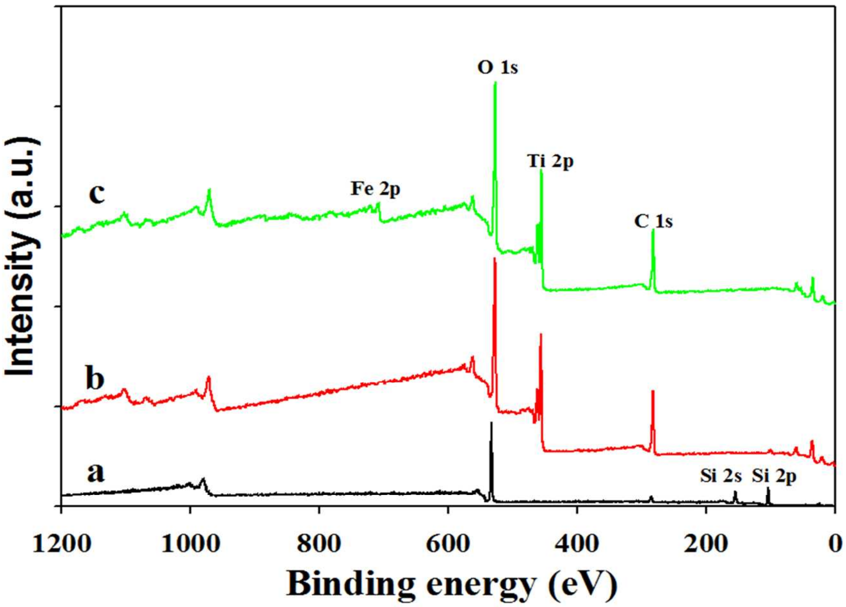

Fig. 6. XPS spectra of (a) the Fe_3O_4@SiO_2 core-shell nanospheres (b) mesoporous Fe_3O_4@SiO_2@mTiO_2-600 core-shell nanospheres, and (c) mesoporous Fe_3O_4@mTiO_2-600 core-shell nanospheres without the silica layer.

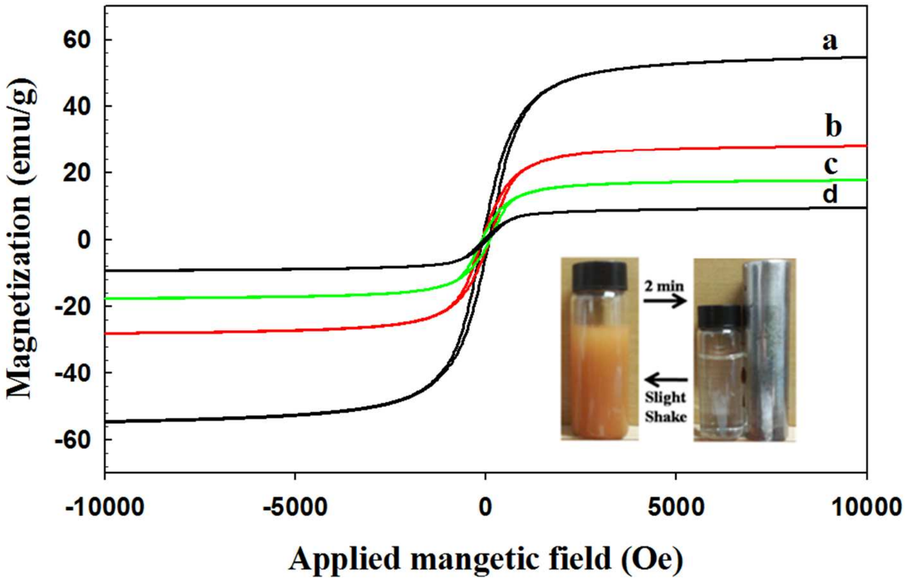

Fig. 7. The magnetic hysteresis loops at 300 K of (a) Fe_3O_4 spheres, (b) Fe_3O_4@SiO_2 core-shell nanospheres, (c) mesoporous Fe_3O_4@SiO_2@mTiO_2-600 core-shell nanospheres, and (d) mesoporous Fe_3O_4@mTiO_2-600 core-shell nanospheres without silica layer. Inset shows the simple magnetic separation process *via* a hand-held magnet.

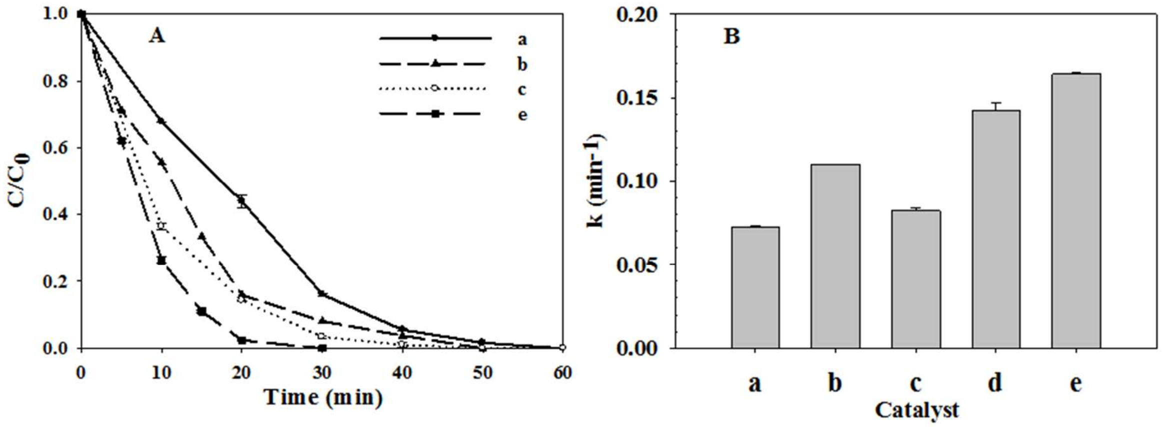

Fig. 8. The sonocatalytic degradation performance of bisphenol-A with varied sonocatalysts: (A) the degradation profiles of BPA and (B) the sonocatalytic degradation kinetic constants. (a) ultrasound alone (b) nonporous $Fe_3O_4@SiO_2@TiO_2$-600 core-shell nanospheres, (c) P25, (d) mesoporous $Fe_3O_4@mTiO_2$-600 core-shell nanospheres without silica layer and (e) mesoporous $Fe_3O_4@SiO_2@mTiO_2$-600 core-shell nanospheres.

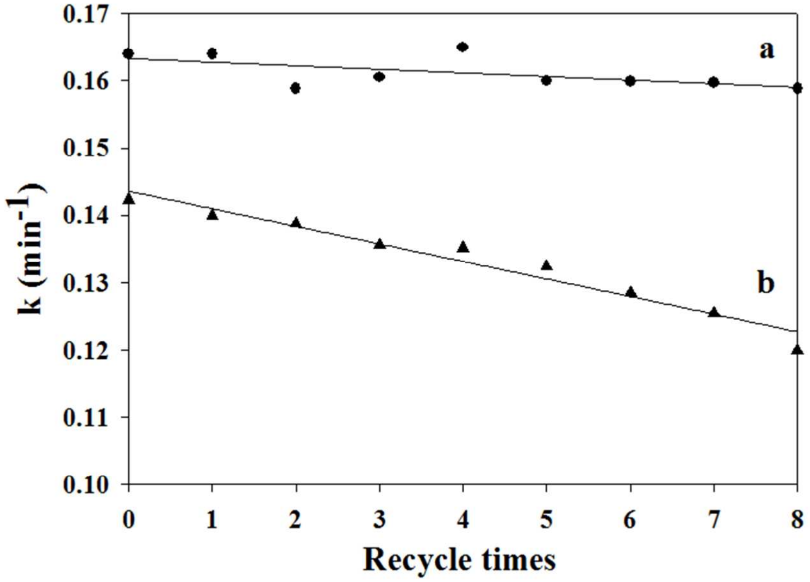

Fig. 9. The recycle performance of (a) the mesoporous Fe_3O_4@SiO_2@mTiO_2-600 core-shell nanospheres and (b) mesoporous Fe_3O_4@mTiO_2-600 core-shell nanospheres without silica layer.

TOC

Uniform core-shell structured magnetic mesoporous TiO_2 as a highly efficient and stable sonocatalyst for the degradation of bisphenol-A.